Targeting Fibroblast Iron Uptake via SLC39A14 Prevents Pathological Tissue Remodeling in Inflammatory Arthritis

Supplementary Figures

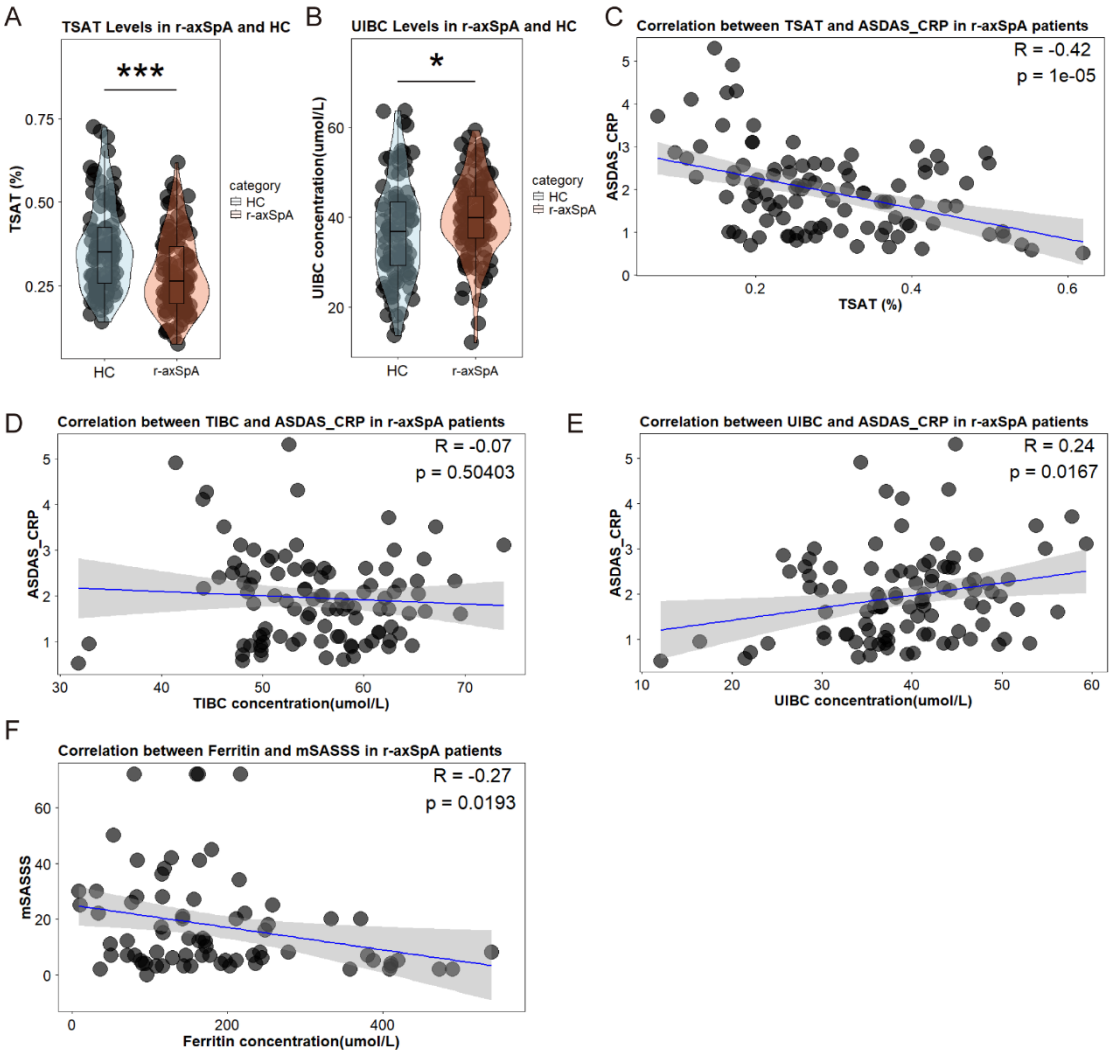

Supplementary Figure S1. Additional iron metabolism parameters and their clinical correlations in r-axSpA

A, B Additional serum iron-related parameters in r-axSpA patients (n = 105) and healthy controls (HCs; n = 95).

(A) Transferrin saturation (TSAT, %).

(B) Unsaturated iron-binding capacity (UIBC, μmol/L).

Data are shown as individual values with violin and box plots (median, IQR). Cohorts were age- and sex-matched; missing values and outliers (IQR method) were excluded. Two-tailed Mann–Whitney U tests. *P < 0.05, **P < 0.01, ***P < 0.001.

C, D, E Correlations between iron-related parameters and disease activity in

r-axSpA patients (n = 105).
(C) Correlation between TSAT and Ankylosing Spondylitis Disease Activity Score based on C-reactive protein (ASDAS-CRP).
(D) Correlation between total iron-binding capacity (TIBC) and ASDAS-CRP.
(E) Correlation between UIBC and ASDAS-CRP.
Spearman's correlation coefficients (R) and P values are shown. Lines indicate linear regression with shaded 95% confidence intervals.

F Correlation between serum ferritin concentration and modified Stoke Ankylosing Spondylitis Spine Score (mSASSS) in a subset of r-axSpA patients with available spinal CT imaging (n = 77). Spearman's correlation (R) and P value are shown; line indicates linear regression with 95% confidence interval.

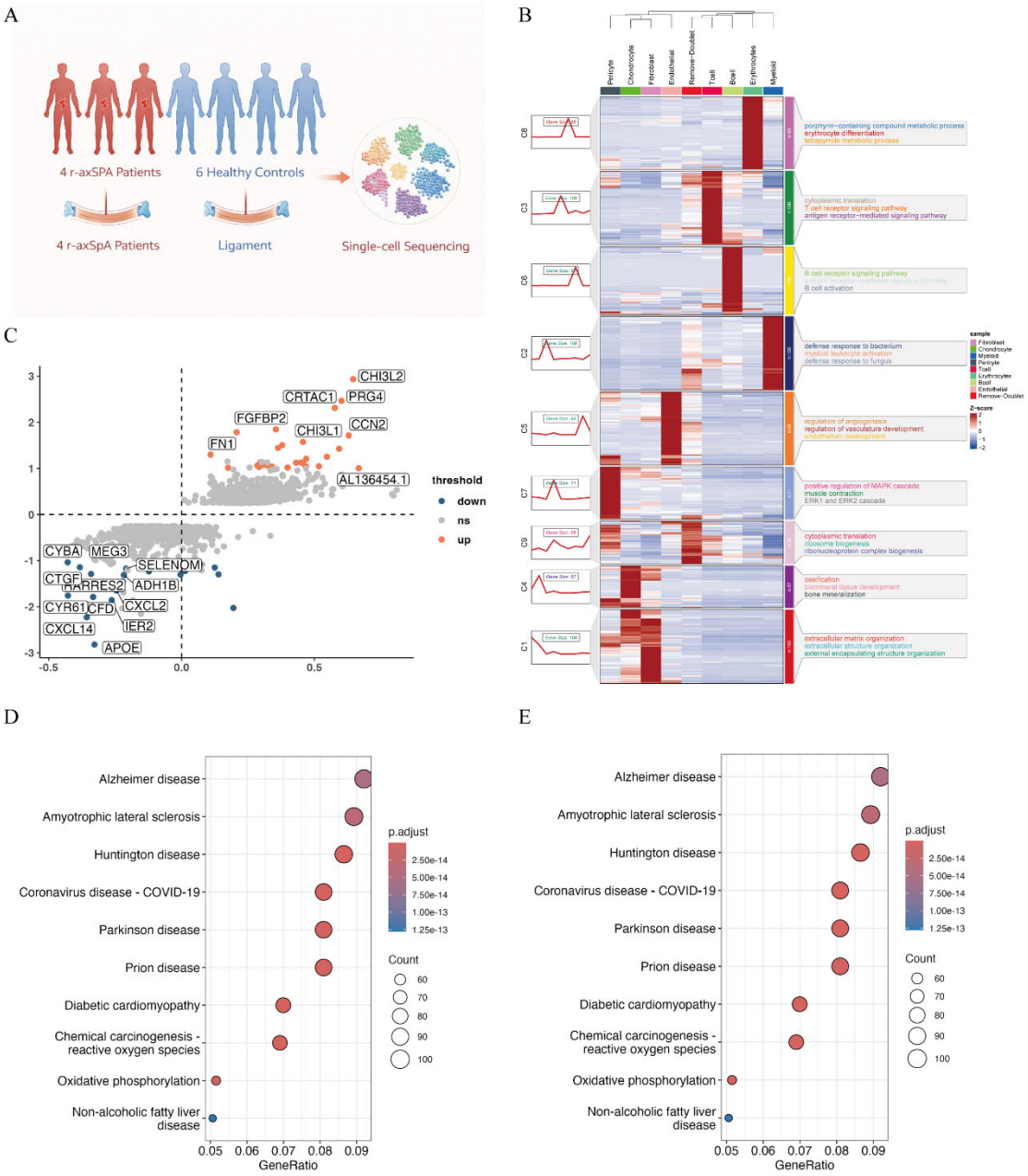

Supplementary Figure S2. Supplemental analyses of single-cell transcriptomics in r-axSpA

A UMAP visualization of single-cell RNA-seq data from ligament tissues of radiographic axial spondyloarthritis (r-axSpA; n = 4 samples) and healthy controls (HCs; n = 6 samples), showing major cell types including fibroblasts, pericytes, endothelial cells, myeloid cells, T cells, and B cells. Cell types were annotated based on canonical marker genes.

B Heatmap of differentially expressed genes (DEGs) between r-axSpA and HCs fibroblasts, highlighting increased expression of selected iron metabolism– and extracellular matrix (ECM)–related genes in r-axSpA fibroblasts. DEGs were identified using Seurat Wilcoxon rank-sum testing

(FDR < 0.05, |log2FC| > 1).

C KEGG pathway enrichment analysis of fibroblast DEGs (defined in B), highlighting pathways related to inflammation, mineral absorption, and ferroptosis.

D, E Dot plots showing cell-type–specific expression patterns of iron metabolism–related genes in myeloid cells (D) and pericytes (E), indicating that few iron metabolism–related genes met the DEG criteria in these compartments compared with fibroblasts.

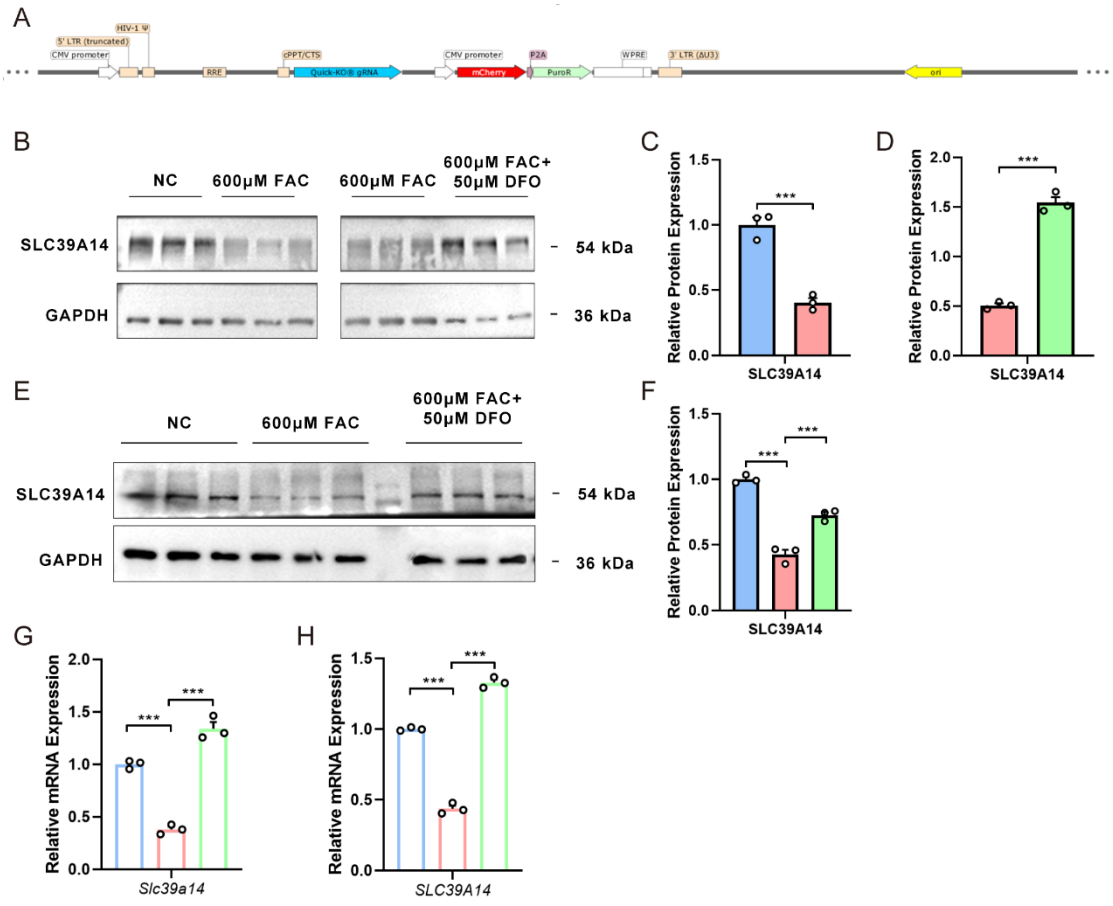

Supplementary Figure S3. Regulation of SLC39A14 Expression in Fibroblasts Under Iron Overload Conditions

A Schematic representation of the CRISPR–Cas9–mediated Slc39a14 knockout strategy in TTD6 fibroblasts.

B, C, D Regulation of SLC39A14 protein expression in mouse fibroblasts following iron loading.
(B) Representative immunoblot of SLC39A14 protein levels in TTD6 fibroblasts treated with ferric ammonium citrate (FAC, 600 μM) with or without deferoxamine (DFO, 50 μM).
(C) Quantification of SLC39A14 protein levels in TTD6 fibroblasts, normalized to GAPDH.
(D) Quantification of the corresponding protein levels, showing the effects of FAC and DFO treatments.

E, F Regulation of SLC39A14 protein expression in primary human ligament fibroblasts under iron overload conditions.
(E) Representative immunoblot of SLC39A14 protein levels in human ligament fibroblasts treated with FAC (600 μM) ± DFO (50 μM).
(F) Quantification of SLC39A14 protein levels in human ligament fibroblasts, normalized to GAPDH.

G *Slc39a14* mRNA expression in TTD6 fibroblasts treated with FAC and DFO, assessed by qRT–PCR and normalized to *GAPDH*.

H *SLC39A14* mRNA expression in primary human ligament fibroblasts under the same treatment conditions, assessed by qRT–PCR and normalized to *GAPDH*.

Data are presented as mean ± s.e.m.; n denotes replicate wells per condition (as indicated in the figure). Statistical significance was assessed using two-tailed unpaired Student's t-tests. Asterisks indicate statistical significance: *P < 0.05, **P < 0.01, ***P < 0.001.

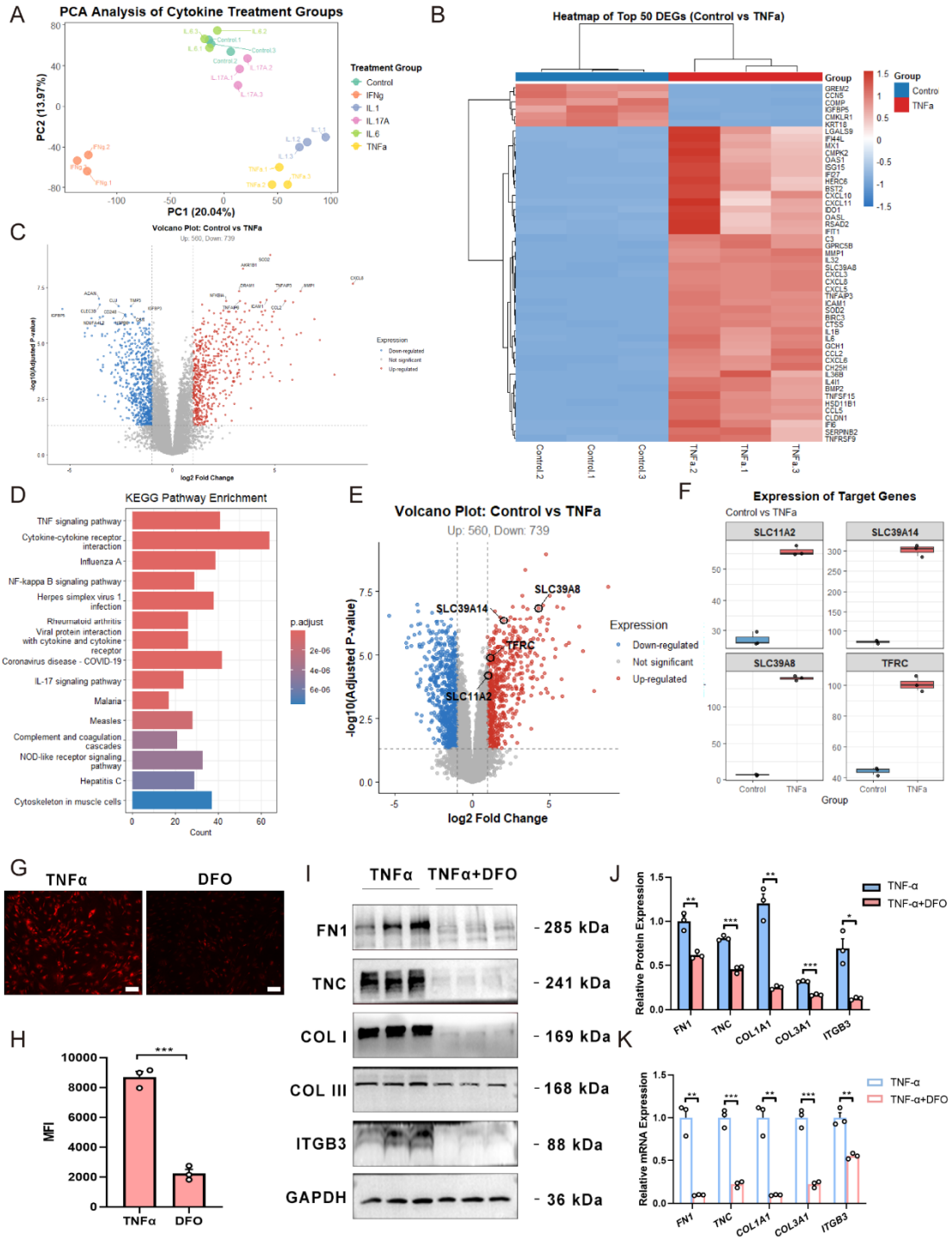

Supplementary Figure S4. TNFα-dependent regulation of iron metabolism and fibrotic responses

A Principal component analysis (PCA) of bulk RNA-seq profiles from primary human spinal ligament fibroblasts treated with the indicated cytokines (IL-1β, IL-6, IL-17A, TNFα, and IFNγ) or untreated controls (n = 3 per condition).

B Heatmap of the top 50 differentially expressed genes (DEGs) comparing TNFα-treated versus control fibroblasts.

C Volcano plot of DEGs for control versus TNFα.

D KEGG pathway enrichment analysis of TNFα-responsive DEGs.

E Volcano plot highlighting selected iron-handling genes (*SLC39A14*, *SLC39A8*, *SLC11A2*, and *TFRC*).

F Expression levels of representative iron transporter genes in control versus TNFα-treated fibroblasts.

G Representative FerroOrange staining showing intracellular labile iron in fibroblasts treated with TNFα with or without deferoxamine (DFO). Scale bars, 200 μm.

H Flow cytometric quantification of FerroOrange mean fluorescence intensity (MFI).

I Immunoblotting of ECM-related proteins (FN1, TNC, COL I, COL III, and ITGB3) in fibroblasts treated with TNFα ± DFO; GAPDH serves as a loading control.

J Densitometric quantification of the immunoblotting results in (I).

K qRT-PCR analysis of ECM-related transcripts in fibroblasts treated with TNFα ± DFO. Statistical significance is indicated as *P < 0.05, **P < 0.01, and ***P < 0.001.

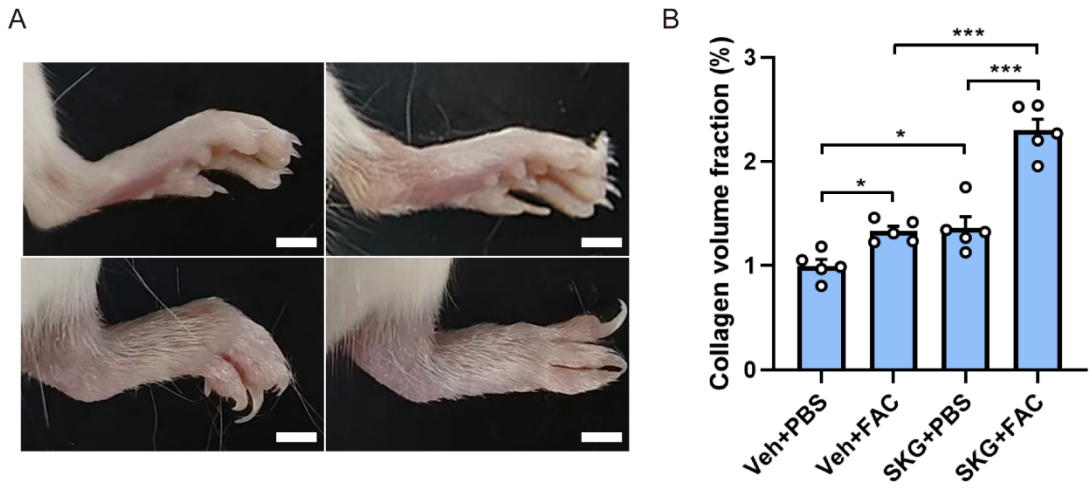

Supplementary Figure S5. Local iron overload aggravates hind paw swelling and collagen deposition in SKG arthritis.

A Representative gross images of hind paws from the four experimental groups (Veh+PBS, Veh+FAC, SKG+PBS, and SKG+FAC) following two intra-articular injections of ferric ammonium citrate (FAC) or phosphate-buffered saline (PBS) during the first week after arthritis induction. Scale bars, 2 mm.

B Quantification of collagen volume fraction (%) in ankle joints from the indicated groups. Each dot represents one mouse (n = 5 per group); bars show mean ± s.e.m. Statistical significance is indicated as *P < 0.05 and ***P < 0.001.

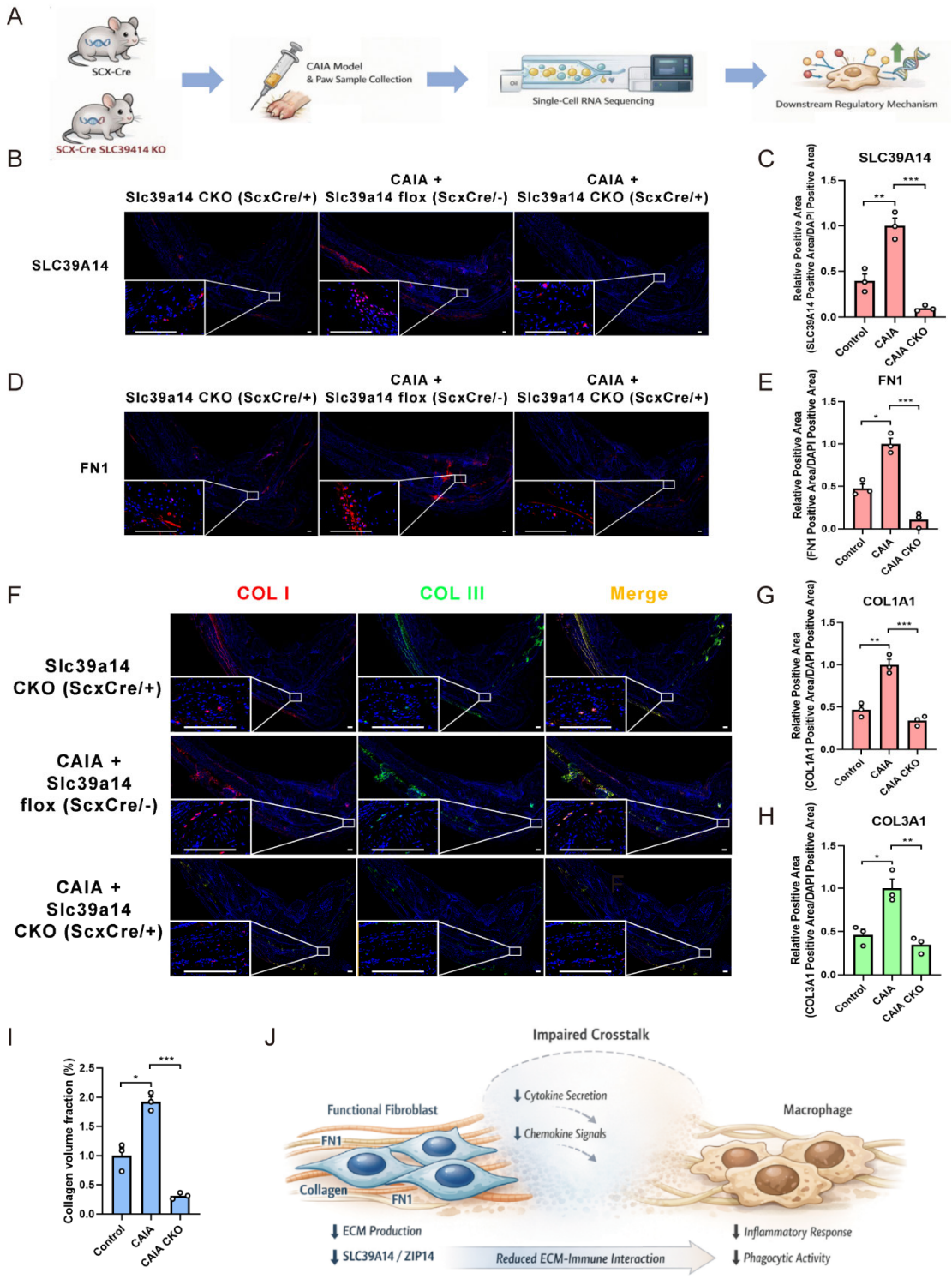

Supplementary Figure S6. Validation of Scx-lineage Slc39a14 deletion and its effects on ECM remodeling

A Workflow schematic for CAIA induction, paw sample collection, scRNA-seq profiling, and downstream analyses.

B Representative immunofluorescence staining of SLC39A14/ZIP14 and FN1 in joint sections from control, CAIA, and CAIA+CKO mice (boxed regions shown at higher magnification in insets). Scale bars, 200 μm.

C, D Quantification of SLC39A14/ZIP14-positive area (C) and FN1-positive area (D), normalized to DAPI-positive area. *P < 0.05, **P < 0.01, ***P < 0.001 by two-tailed unpaired t-test.

E Co-immunofluorescence staining of COL I (red) and COL III (green) with merged images across groups. Scale bars, 200 μm.

F, G Quantification of COL3A1-positive area (F) and COL1A1-positive area (G), normalized to DAPI-positive area. *P < 0.05, **P < 0.01, ***P < 0.001 by two-tailed unpaired t-test.

H Model summarizing that loss of fibroblast SLC39A14/ZIP14 reduces ECM production and impairs pathological stromal–immune crosstalk, thereby attenuating inflammatory amplification and tissue remodeling.

I Quantification of collagen volume fraction in joint sections from control, CAIA, and CAIA+CKO mice. Data are presented as percentage of total tissue area. P values are derived from two-tailed unpaired t-test.

J Diagram illustrating that loss of SLC39A14/ZIP14 in fibroblasts disrupts the ECM remodeling process by impairing stromal-immune crosstalk, which in turn reduces ECM production and attenuates inflammatory amplification and tissue remodeling.

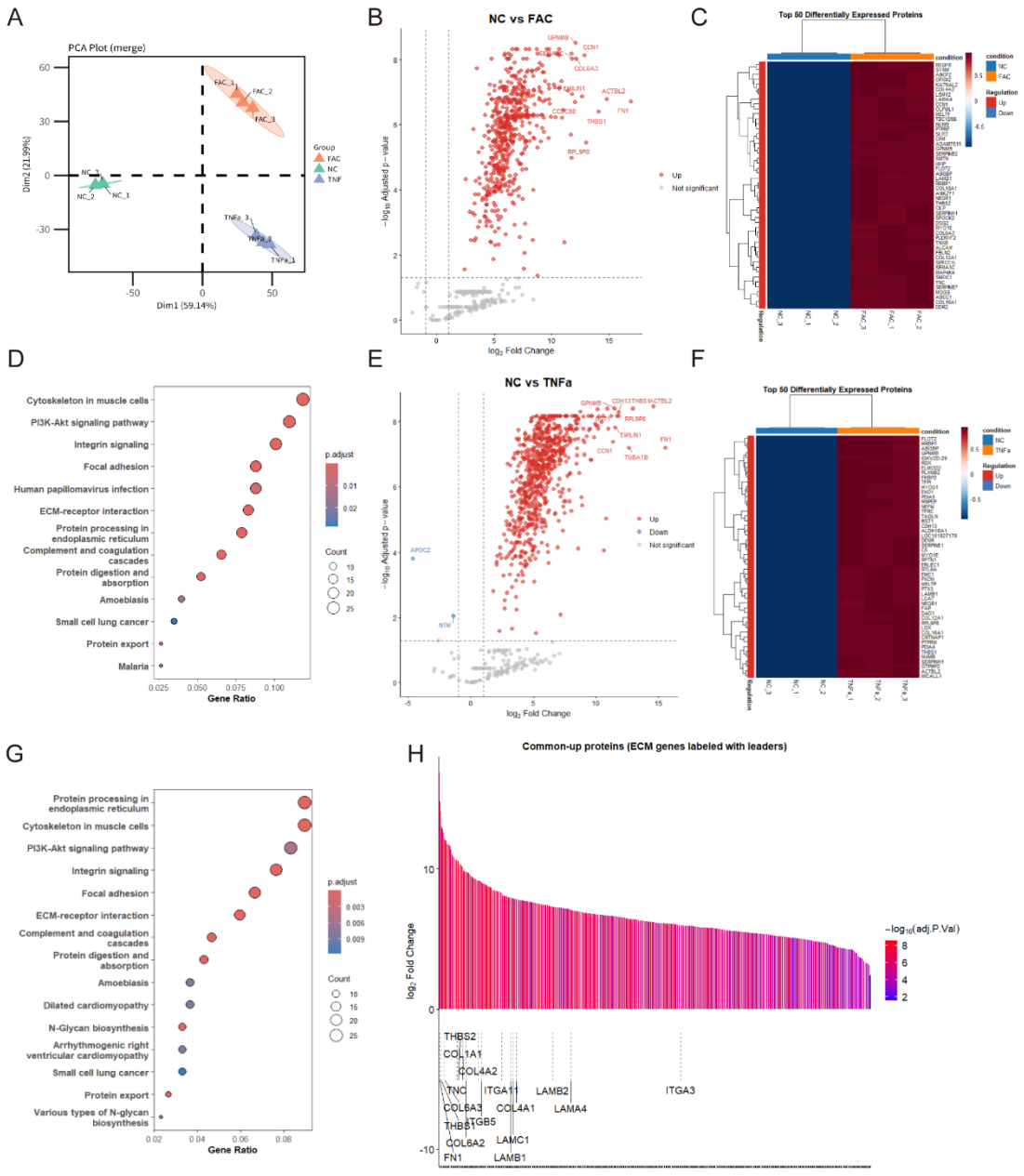

Supplementary Figure 7. Proteomic Analysis of ECM Conditioned by FAC and TNFα Treatments

A PCA plot illustrating the proteomic profiles of ECM derived from fibroblasts treated with FAC and TNFα, compared to normal control (NC). The plot demonstrates clear separation between the three groups, indicating distinct proteomic changes in response to the treatments.

B Volcano plot comparing differential protein expression in ECM from FAC-treated fibroblasts relative to NC. The plot shows significant upregulation of multiple ECM-related proteins, highlighting key proteins such as COL1A1

and FN1.

C Heatmap of the top 50 differentially expressed proteins in ECM derived from FAC-treated fibroblasts compared to NC. The proteins are clustered based on expression patterns, with ECM-related proteins showing substantial upregulation in FAC-treated ECM.

D KEGG pathway enrichment analysis of the upregulated proteins in ECM derived from FAC-treated fibroblasts. Significant pathways include ECM-receptor interaction, focal adhesion, and PI3K-Akt signaling pathway, suggesting alterations in ECM dynamics and cell signaling.

E Volcano plot comparing differential protein expression in ECM from TNFα-treated fibroblasts relative to NC. Similar to the FAC treatment, significant upregulation of ECM-related genes such as *COL1A1* and *FN1* is observed.

F Heatmap of the top 50 differentially expressed proteins in ECM derived from TNFα-treated fibroblasts compared to NC. The heatmap shows a pattern of upregulated ECM-related proteins in TNFα-conditioned ECM.

G KEGG pathway enrichment analysis of the upregulated proteins in ECM derived from TNFα-treated fibroblasts. Enriched pathways include ECM-receptor interaction, focal adhesion, and PI3K-Akt signaling pathway, highlighting the common signaling mechanisms activated by both FAC and TNFα treatments.

H Waterfall plot showing the top upregulated ECM-related proteins common to both FAC and TNFα treatments. ECM genes like *FN1*, *COL1A1*, and *LAMC1* are highlighted, with *FN1* showing the highest fold change.